Journal of Inorganic and Organometallic Polymers and Materials
https://doi.org/10.1007/s10904-023-02727-4

RESEARCH

Photocatalytic Decomposition of Indigo Carmine and Methylene Blue Dyes using Facilely Synthesized Lithium Borate/Copper Oxide Nanocomposite

Nada S. Al-Kadhi[1] · Fawaz A. Saad[2] · Reem K. Shah[2] · Gharieb S. El-Sayyad[3,4] · Zahrah Alqahtani[5] · Ehab A. Abdelrahman[6,7]

Received: 22 April 2023 / Accepted: 18 May 2023

Abstract

The leakage of factories that contain methylene blue and indigo carmine dyes into water sources causes some health problems, such as skin infections, cancer, and digestive system troubles. Consequently, in this work, a lithium borate/copper oxide nanocomposite was facilely synthesized using the pechini sol gel method. After that, the synthesized nanocomposite was used for the remarkable photocatalytic decomposition of indigo carmine and methylene blue dyes. The combination of lithium borate with copper oxide prevents fast recombination of hole/electron pairs and thus increases the efficiency of photocatalytic decomposition of indigo carmine and methylene blue dyes. This is because the interfacial charge transfer efficiency and separation of photo-generated products are dramatically improved by the combination of lithium borate with copper oxide. The synthesized nanocomposite was characterized using an ultraviolet–visible spectrophotometer (UV-Vis spectrophotometer), Fourier-transform infrared spectroscopy (FT-IR), field emission scanning electron microscopy (FE-SEM), X-ray powder diffraction (XRD), and high-resolution transmission electron microscopy (HR-TEM). The average crystallite size of the synthesized nanocomposite is 18.58 nm. The synthesized nanocomposite has two optical energy gap (E_g) values of 2.67 and 5 eV due to CuO and Li_3BO_3 phases, respectively. In addition, the FE-SEM and HR-TEM images showed that the synthesized nanocomposite consists of polyhedral, irregular, and rod-like structures with average diameters of 237.83 and 15.75 nm, respectively. The highest decomposition percentages of 100 mL of 25 mg/L of the methylene blue (at pH = 9) and indigo carmine (at pH = 3) dyes using 0.05 g of the synthesized nanocomposite are 93.03 and 89.13%, respectively.

Keywords Photocatalytic degradation · Nanocomposites · Indigo carmine dye · Methylene blue dye

✉ Ehab A. Abdelrahman
EAAAhmed@imamu.edu.sa; dr.ehabsaleh@yahoo.com

[1] Department of Chemistry, College of Science, Princess Nourah Bint Abdulrahman University, P.O. Box 84428, Riyadh 11671, Saudi Arabia

[2] Department of Chemistry, Faculty of Applied Sciences, Umm Al-Qura University, Makkah 21955, Saudi Arabia

[3] Microbiology and Immunology Department, Faculty of Pharmacy, Ahram Canadian University (ACU), Giza, Egypt

[4] Microbiology and Immunology Department, Faculty of Pharmacy, Galala University, Galala City, Suez, Egypt

[5] Department of Physics, Faculty of Science, Taif University, P.O. Box 11099, Taif 21944, Saudi Arabia

[6] Department of Chemistry, College of Science, Imam Mohammad Ibn Saud Islamic University (IMSIU), Riyadh 11623, Saudi Arabia

[7] Chemistry Department, Faculty of Science, Benha University, Benha 13518, Egypt

1 Introduction

Urbanization and industrialization are the primary causes of the discharge of large quantities of hazardous materials, which contaminate the environment and ecosystem. Major contributors to water pollution are effluents from textile industries, which are chemically intensive and contain high concentrations of complex chemical components such as heavy metals and dyes [1–6]. Methylene blue and indigo carmine are cationic and anionic dyes, respectively. They are used in various industrial applications and as a pharmaceutical additive for medical diagnosis. For both humans and aquatic animals, these dyes can cause a variety of health problems, including ocular irritation, skin diseases, vomiting, diarrhea, cancer, hypertension, nervous system disturbances, and gastrointestinal infections [7–10]. Many approaches have been demonstrated for the removal of several organic dyes, like precipitation, nanofiltration, reverse osmosis, coagulation/flocculation, adsorption, and photocatalytic decomposition [11–19]. Due to the escalating environmental challenges, photocatalytic decomposition of environmental contaminants has lately gained great attention. Because it is an economical, eco-friendly, dependable, and repeatable method, photocatalytic decomposition is primarily utilized for the removal of hazardous water or air pollutants. In the photocatalytic decomposition method, it is well known that both light and catalyst play a role, but the catalyst is the most crucial factor because it affects the efficiency of the decomposition. If the catalyst is exposed to light, electronic transitions occur from the valence band to the conduction band, which results in holes and electrons, which in turn produce free radicals that break down the organic dyes [15, 20–25]. Due to their promising applications in water treatment, semiconducting photocatalysts have garnered a great deal of consideration from scientists and have rapidly improved over the past few years. There are a lot of photocatalysts that were utilized for the decomposition of organic dyes, for example, titanium oxide, barium titanate, cerium oxide, graphitic carbon nitride, and zirconium phosphate [26–31]. It is well known that a low recombination rate of yielded hole/electron pairs and high removal efficiency are required to perform effective photocatalytic decomposition reactions of organic contaminants under ultraviolet light irradiation. Due to their distinctive applications in water splitting, nonlinear optical devices, photo-luminescent substances, lithium-ion batteries, plasma and laser technology, photocatalytic areas, and the adsorption of carbon dioxide, borate-based nanocrystalline semiconductors have attracted significant attention in recent years. In addition, it has been reported that lithium-borate composites have a perovskite-like structure that demonstrates significant property-structure correlations [32–35]. Nevertheless, the Li_3BO_3 substance has a large optical band energy gap (approximately 5 eV), which severely restricts the photocatalytic decomposition property of the Li_3BO_3 substance. By connecting two semiconductors with suitable optical band gaps, the performance of semiconductor photocatalysts can be significantly enhanced because the interfacial charge transfer efficiency and separation of photo-generated products are dramatically improved [36, 37]. Copper oxides (including Cu_2O and CuO) as semiconductors of the p-type with small optical band energy gaps have gotten a great deal of attention over the past decade due to their numerous uses in solar cells, sensors, superconductors, catalysis, and electrode materials. Due to its small optical band gap, high abundance, and non-toxicity, CuO has been widely utilized in the photocatalytic decomposition of several pollutants. Consequently, CuO with a very narrow optical band energy gap of approximately 2 eV can almost absorb the majority of ultraviolet light and boost the photocatalytic decomposition property of Li_3BO_3 by enhancing the efficiency of photogenerated holes/electrons separation [38–40]. The sol-gel technique of the pechini type relies on the formation of chelates between ligands such as citric acid and metal ions. After that, the transesterification was carried out using cross-linking agents such as polyethylene glycol 400 to obtain the polymeric complex network. By heating the polymeric complex network, it is possible to remove the organic part and obtain metal oxide nanoparticles. This procedure has numerous benefits, including the use of non-toxic chemicals, a low temperature, and the ability to easily organize the process environment. The pechini sol-gel chemical method was utilized for the synthesis of several nanoparticles, for example, lithium niobate, magnesium oxide, aluminum oxide, magnesium ferrite, $MgMn_2O_4/Mn_2O_3$ composite, $MgMn_2O_4/Mn_2O_3/Mg_6MnO_8$ composite, $Mn_{0.5}Zn_{0.5}Fe_2O_4/Fe_2O_3$ composite, and $Fe_{0.5}Mn_{0.5}Co_2O_4/Fe_2O_3$ composite [23, 25, 41–45]. Salavati-Niasari et al. synthesized some efficient photocatalysts, such as erbium vanadate, $Fe_2O_3/EuVO_4/g\text{-}C_3N_4$ nanocomposite, Co/Co_3O_4 nanocomposite, $BaDy_2NiO_5/NiO$ nanocomposite,$BaDy_2NiO_5/Dy_2O_3$nanocomposite,$DyBa_2Fe_3O_{7.988}/DyFeO_3$ nanocomposite, $Dy_2BaCuO_5/Ba_4DyCu_3O_{9.09}$ nanocomposite, $Ni/Ni(OH)_2$ nanocomposite, and Tb-Co-O nanostructures for the decomposition of some organic dyes [46–53]. Despite the high efficiency of these catalysts, the chemicals used to prepare them are very expensive. Therefore, the first innovative aspect of our paper comes from the ability of our research team to utilize low-cost chemicals for synthesizing a lithium borate/copper oxide nanocomposite by the pechini sol-gel method. The second innovative aspect of our paper comes from the efficient decomposition of dangerous pollutants such as methylene blue and indigo carmine dyes using the synthesized nanocomposite as a photocatalyst. The

combination of copper oxide with lithium borate prevents rapid recombination of holes/electrons and accordingly increases the efficiency of photocatalytic decomposition of methylene blue and indigo carmine dyes. Moreover, in the current paper, the impacts affecting the photocatalytic decomposition of indigo carmine and methylene blue dyes using the synthesized nanocomposite as a catalyst were also studied.

2 Experimental

2.1 Chemicals

Lithium sulfate monohydrate ($Li_2SO_4{\cdot}H_2O$), boric acid (H_3BO_3), copper(II) nitrate trihydrate ($Cu(NO_3)_2{\cdot}3H_2O$), sodium hydroxide (NaOH), polyethylene glycol 400 ($C_{2n}H_{4n+2}O_{n+1}$), citric acid monohydrate ($C_6H_8O_7.H_2O$), indigo carmine dye ($C_{16}H_8N_2Na_2O_8S_2$), methylene blue dye ($C_{16}H_{18}ClN_3S$), ethylenediaminetetracetic acid disodium salt dihydrate ($C_{10}H_{14}N_2Na_2O_8{\cdot}2H_2O$), ascorbic acid ($C_6H_8O_6$), isopropyl alcohol ($C_3H_8O$), and hydrochloric acid (HCl) were of analytical grade (Purity = 99.999%), gotten from the Merck chemical company, and utilized without any refining.

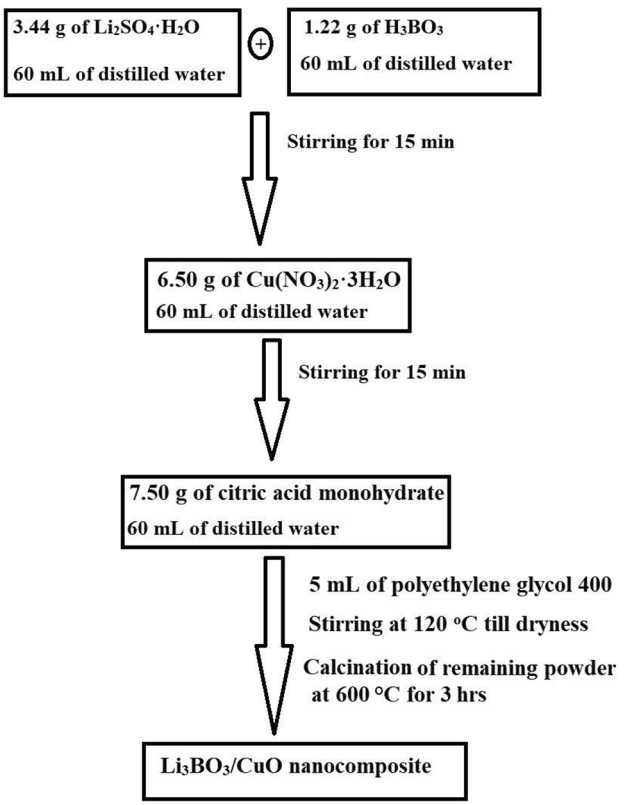

Scheme 1 Graphical presentation for the synthesis of the Li_3BO_3/CuO nanocomposite

2.2 Synthesis of Li_3BO_3/CuO Nanocomposite

3.44 g of $Li_2SO_4{\cdot}H_2O$ was dissolved in 60 mL of distilled water. Besides, 1.22 g of H_3BO_3 was dissolved in 60 mL of distilled water. In addition, the above two metallic solutions were mixed with each other and then magnetically stirred for 15 min. 6.50 g of $Cu(NO_3)_2{\cdot}3H_2O$ was dissolved in 60 mL of distilled water then added to the previous mixture with constant stirring for 15 min. After that, the citric acid solution, which was prepared by dissolving 7.50 g of citric acid monohydrate in 60 mL of distilled water, was added with constant stirring for 15 min. In addition, 5 mL of polyethylene glycol 400 was added then the mixture was magnetically stirred at 120 °C till dryness. Lastly, the generated powder was calcined in muffle at 600 °C for 3 h. Scheme 1 shows the practical steps for synthesizing the Li_3BO_3/CuO nanocomposite.

2.2.1 Characterization

The FT-IR spectrum of the synthesized nanocomposite was obtained in the range 4000 – 400 cm^{-1} using a Nicolet iS50 spectrophotometer. The XRD pattern of the synthesized nanocomposite was obtained using a D8 Advance X-ray diffractometer with a copper anode (λ of CuK_α=1.5 Å). The surface morphology of the synthesized nanocomposite was investigated using a FE-SEM of model JSM-IT800 Schottky attached to an energy-dispersive X-ray unit (EDX). The morphology of the synthesized nanocomposite was investigated by a HR-TEM of the model Talos F200iS. In addition, the concentration of the methylene blue and indigo carmine dyes was measured by a UV/Vis spectrophotometer of the model Shimadzu UV-1650 PC. Moreover, the lambda max of the methylene blue and indigo carmine dyes is 663 and 610 nm, respectively.

2.3 Photocatalytic Decomposition of Methylene Blue and Indigo Carmine Dyes using the Li_3BO_3/CuO Nanocomposite

For the purpose of determining the photocatalytic activity of Li_3BO_3/CuO nanocomposite, methylene blue and indigo carmine dyes were decomposed in the presence of two ultraviolet lamps of the same type (Wavelength = 240 nm). In this regard, 0.05 g of the Li_3BO_3/CuO nanocomposite was added to 100 mL of original concentration of 25 mg/L methylene blue or indigo carmine dye aqueous solution then the suspension was stirred for 2 h in the absence of an ultraviolet light to achieve adsorption/desorption equilibrium. It is worth noting that the adsorption in the dark was followed up at different times, and it was found that equilibrium occurred after 2 h. In addition, the obtained mixture was

then subjected to an ultraviolet light irradiation. The effects of pH (3–9), irradiation time (10–110 min), amount of nanocomposite (0.0125-0.2 g), and concentration of dye (15–35) were studied. The percentage of photocatalytic decomposition (% D) of indigo carmine or methylene blue dyes was estimated by Eq. (1).

$$\%D = \frac{C_d - C_e}{C_d} \times 100 \quad (1)$$

where, C_d (mg/L) is the concentration of methylene blue or indigo carmine dyes after the adsorption in the dark place. C_e (mg/L) is the concentration of methylene blue or indigo carmine dyes after illumination with an ultraviolet light.

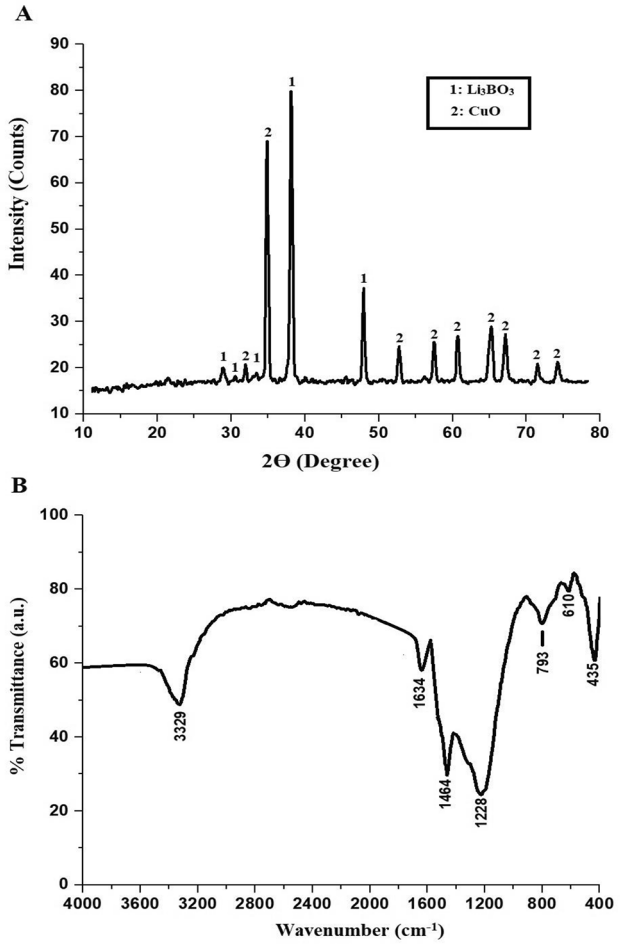

Fig. 1 The XRD pattern (**A**) and FT-IR spectrum (**B**) of the synthesized nanocomposite

3 Results and Discussion

3.1 Characterization of the Synthesized Nanocomposite

Figure 1 A represents the XRD pattern of the synthesized nanocomposite. The results confirmed that the synthesized nanocomposite consists of lithium borate (Li_3BO_3) and copper(II) oxide (CuO) as clarified in JCPDS Nos. 70-2459 and 80-1917, respectively [54, 55]. The peaks, which appeared at 2Θ=28.90°, 30.65°, 33.41°, 38.09°, and 47.92°, are due to the Li_3BO_3 compound. Also, the peaks, which appeared at 2Θ=31.94°, 34.88°, 52.79°, 57.46°, 60.67°, 65.09°, 67.10°, 71.51°, and 74.21°, are due to the CuO compound. The average crystallite size of the synthesized nanocomposite, which was determined using Scherrer equation, is 18.58 nm [44, 56–59]. In addition, the percentages of Li_3BO_3 and CuO are 40 and 60%, respectively.

Figure 1B represents the FT-IR spectrum of the synthesized nanocomposite. The results showed that the bands, centered at 435 and 610 cm^{-1}, were assigned to the stretching vibrations of the Li-O and Cu-O, respectively. In addition, the band, centered at 793 cm^{-1}, was assigned to the bending vibration of the B-O-B. The band, centered at 1228 cm^{-1}, was assigned to the stretching vibrations of boron tetrahedral structural units. The band, centered at 1464 cm^{-1}, was assigned to the asymmetric stretching vibration of BO_3. The bands, centered at 1634 and 3329 cm^{-1}, were assigned to the bending and stretching vibrations of adsorbed water, respectively [60–68].

Figure 2 A-B represents the FE-SEM and HR-TEM images of the synthesized nanocomposite, respectively. In addition, the FE-SEM and HR-TEM images showed that the synthesized nanocomposite consists of polyhedral, irregular, and rod-shaped particles with average diameters of 237.83 and 15.75 nm, respectively. High-resolution transmission electron microscopy is an imaging mode of specialized transmission electron microscopes that permits direct imaging of the atomic structure of samples. The interlayer lamellar distances of 0.25 and 0.33 nm were in accord with the lattice fringes of CuO and Li_3BO_3 structures, respectively, which were in excellent agreement with the results of XRD.

The optical energy gap (E_g) of the synthesized nanocomposite (Li_3BO_3/CuO) was determined from the UV–Vis absorption spectra in nujoll mull by Eq. (2) [25].

$$(\sigma h\upsilon)^{Y} = K_E\,(h\upsilon - E_g) \quad (2)$$

K_E and σ are an energy-independent constant and the absorption coefficient, respectively. h and Y are the Planck's constant and an integer depending on the kind of transition, respectively. Y equals 2.0 and 0.5 in the case of direct

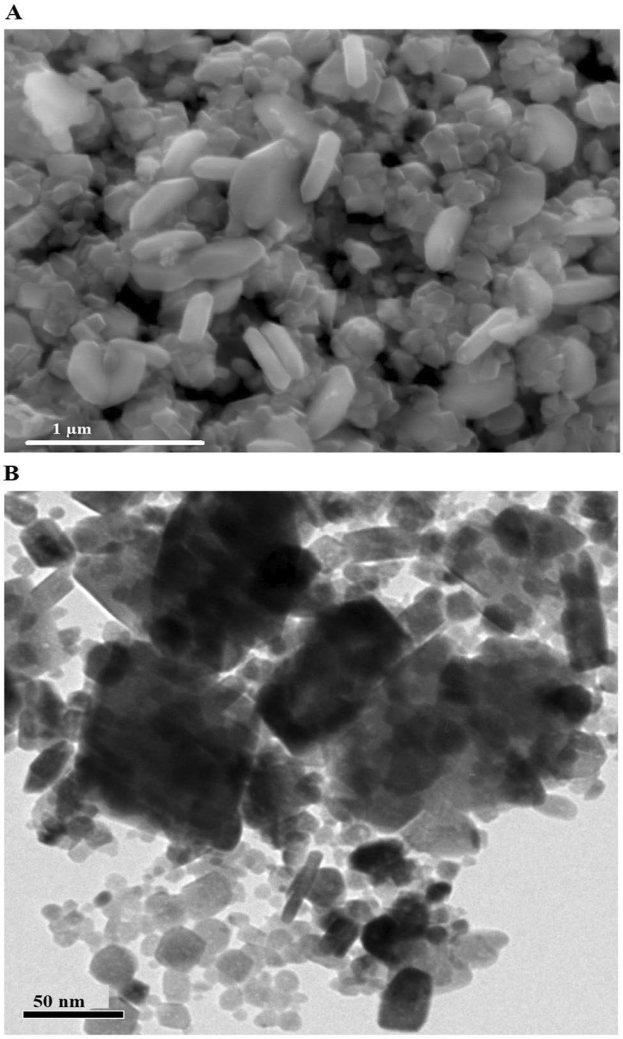

Fig. 2 The FE-SEM (**A**) and HR-TEM (**B**) images of the synthesized nanocomposite

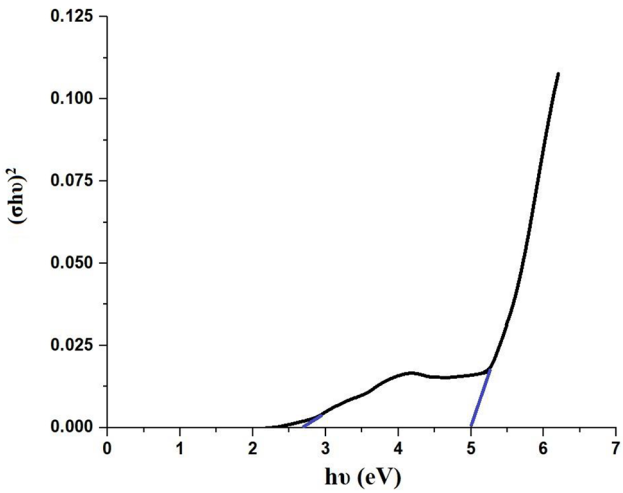

Fig. 3 The optical energy gap of the synthesized nanocomposite

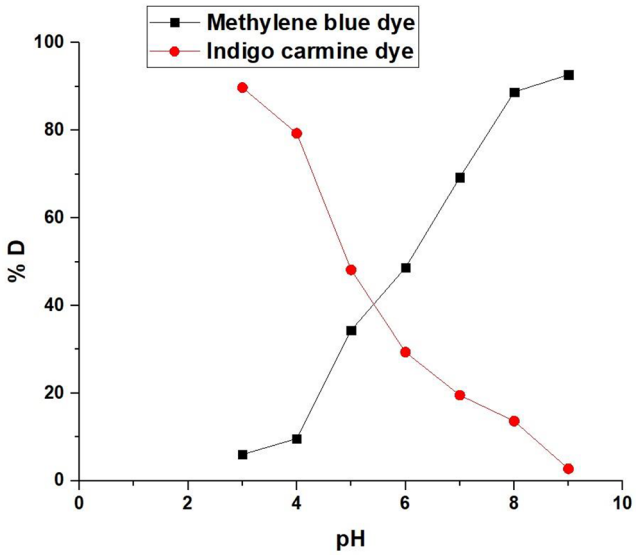

Fig. 4 The effect of pH on the photocatalytic decomposition percentage of 100 mL of 25 mg/L indigo carmine or methylene blue dyes using 0.05 g of the synthesized nanocomposite

allowed and indirect allowed electronic transitions, respectively. Figure 3 shows the plot of $(\sigma h\upsilon)^2$ against hυ for the synthesized nanocomposite. Therefore, the direct allowed electronic transitions were predominant in the synthesized nanocomposite. The extrapolation of the graph until the value of $(\sigma h\upsilon)^2$ equals zero gives the optical energy gap (E_g). There are two optical energy gap values of 2.67 and 5 eV due to the CuO and Li_3BO_3 phases, respectively.

3.2 Photocatalytic Decomposition of Methylene Blue and Indigo Carmine Dyes

3.2.1 Influence of Dye Solution pH

Figure 4 shows the relationship between the pH and the photocatalytic decomposition percentage of indigo carmine and methylene blue dyes in the presence of ultraviolet light. In the case of methylene blue dye, when the pH is increased from 3 to 9, the photocatalytic decomposition percentage increases from 6.02 to 92.60%. The acidic medium works to surround the nanocomposite with positive hydrogen ions that expel the cationic methylene blue dye, and thus the photocatalytic decomposition percentage decreases [69]. The basic medium works to surround the nanocomposite with negative hydroxide ions that attract the cationic methylene blue dye, and thus the photocatalytic decomposition percentage increases. In the case of indigo carmine dye, when the pH is increased from 3 to 9, the photocatalytic decomposition percentage decreases from 89.77 to 2.75% [69]. The acidic medium works to surround the nanocomposite with positive hydrogen ions that attract the anionic indigo

carmine dye, and thus the photocatalytic decomposition percentage increases. The basic medium works to surround the nanocomposite with negative hydroxide ions that expel the anionic indigo carmine dye, and thus the photocatalytic decomposition percentage decreases. Therefore, the optimal pH values, for obtaining the highest decomposition percentage of the indigo carmine and methylene blue dyes, are 3 and 9, respectively. The decomposition percentages of indigo carmine and methylene blue dyes in a real wastewater sample, which was taken from our research laboratory wastewater, at optimum conditions were 82.53 and 70.12%, respectively. Compared to the experimentally prepared sample, the decomposition percentage of the studied dyes in the wastewater decreased due to the various kinds of dyes contained in the wastewater and the higher concentration of opaques in the solution.

3.2.2 Influence of Ultraviolet Irradiation Time

Figure 5 A shows the relationship between the ultraviolet irradiation time and the photocatalytic decomposition percentage of indigo carmine and methylene blue dyes. In the case of methylene blue dye, when the ultraviolet irradiation time is increased from 10 to 90 min, the photocatalytic decomposition percentage increases from 7.41 to 93.03%. It was found that the photocatalytic decomposition percentage of methylene blue dye was almost unaffected by increasing the ultraviolet irradiation time from 90 to 110 min due to the saturation of the active sites. In the case of indigo carmine dye, when the ultraviolet irradiation time is increased from 10 to 90 min, the photocatalytic decomposition percentage increases from 4.69 to 89.13%. It was found that the photocatalytic decomposition percentage of indigo carmine dye was almost unaffected by increasing the ultraviolet irradiation time from 90 to 110 min owing to the saturation of the active positions. Therefore, 90 min is considered the optimal value for obtaining the highest decomposition percentage of the methylene blue and indigo carmine dyes. In addition, the catalytic decomposition of the indigo carmine and methylene blue dyes follows well the first order, which is expressed by Eq. 3 [69], as shown in Fig. 5B.

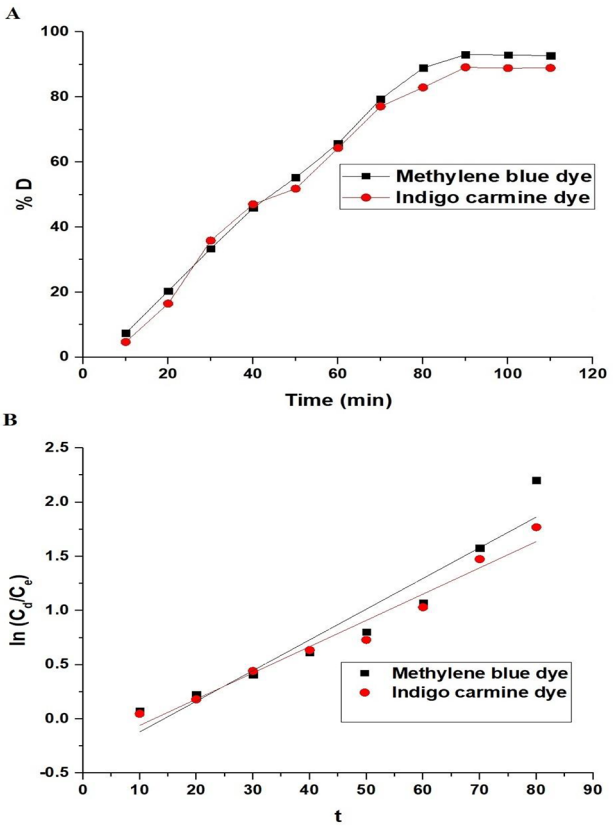

Fig. 5 The effect of ultraviolet irradiation time on the photocatalytic decomposition percentage of 100 mL of 25 mg/L indigo carmine (at pH 3) or methylene blue (at pH 9) dyes using 0.05 g of the synthesized nanocomposite. The first order kinetic model (B)

$$\ln \frac{C_d}{C_e} = K_P t \tag{3}$$

K_P represents the rate constant of the first order (1/min).

The linear fitting of the obtained points in the case of indigo carmine and methylene blue dyes produced lines with a large correlation coefficient, which equals 0.9616 and 0.9142, respectively. The values of K_P in the cases of indigo carmine and methylene blue dyes are 0.0243 and 0.0283 1/min, respectively.

3.2.3 Influence of the Amount of Nanocomposite

Figure 6 shows the relationship between the amount of nanocomposite and the photocatalytic decomposition percentage of indigo carmine and methylene blue dyes. In the case of methylene blue dye, when the amount of nanocomposite is increased from 0.0125 to 0.05 g, the photocatalytic decomposition percentage increases from 47.16 to 93.03% due to the increase in free radicals. Besides, when the amount of nanocomposite is increased from 0.05 to 0.2 g, the photocatalytic decomposition percentage decreases from 93.03 to 80.12% due to the turbidity that blocks the access of light into solution and reduces the number of free radicals. In the case of indigo carmine dye, when the amount of nanocomposite is increased from 0.0125 to 0.05 g, the photocatalytic decomposition percentage increases from 38.54 to 89.13% due to the increase in free radicals. Besides, when the amount of nanocomposite is increased from 0.05 to 0.2 g, the photocatalytic decomposition percentage decreases from 89.13 to 78.00% due to the turbidity that blocks the access of light into solution and reduces the number of free

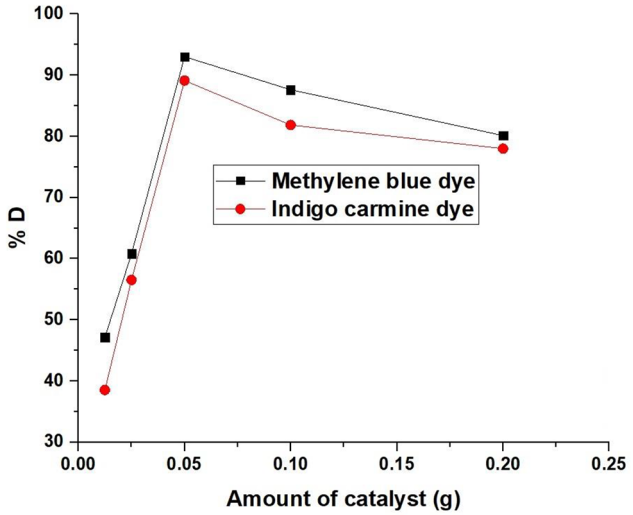

Fig. 6 The effect of the amount of nanocomposite on the photocatalytic decomposition percentage of 100 mL of 25 mg/L indigo carmine (at pH 3) or methylene blue (at pH 9) dyes after 90 min

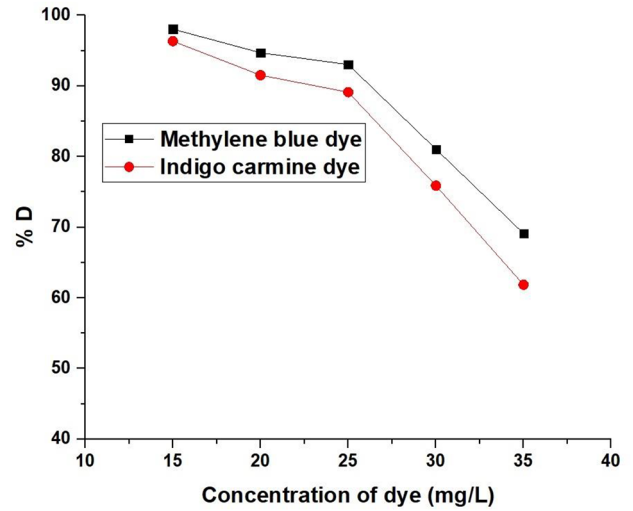

Fig. 7 The effect of the initial dye concentration on the photocatalytic decomposition percentage of 100 mL of indigo carmine (at pH 3) or methylene blue (at pH 9) dyes after 90 min using 0.05 g of the synthesized nanocomposite

radicals. Therefore, the optimal value, for obtaining the highest decomposition percentage of the indigo carmine and methylene blue dyes, is 0.05 g.

3.2.4 Influence of Initial Dye Concentration

Figure 7 shows the relationship between the initial concentration of indigo carmine and methylene blue dyes and the photocatalytic decomposition percentage. In the case of methylene blue dye, when the initial concentration is increased from 15 to 35 mg/L, the photocatalytic decomposition percentage decreases from 98.04 to 69.11% because the high concentration of methylene blue dye blocks the access of light into the nanocomposite. In the case of indigo carmine dye, when the initial concentration is increased from 15 to 35 mg/L, the photocatalytic decomposition percentage decreases from 96.33 to 61.85% because the high concentration of indigo carmine dye blocks the access of light into the nanocomposite.

3.2.5 Mechanism of Photocatalytic Decomposition of Indigo Carmine and Methylene Blue Dyes

Scheme 2 represents the mechanism of photocatalytic decomposition of methylene blue and indigo carmine dyes by the Li_3BO_3/CuO nanocomposite. Ultraviolet light falls on the Li_3BO_3/CuO nanocomposite, causing some electrons to move from the valence band to the conduction band in both Li_3BO_3 and CuO compounds. As a result, electrons are created in the conduction band, while holes are created in the valence band. The combination of Li_3BO_3 with CuO prevents fast recombination of holes/electrons and thus increases the efficiency of photocatalytic decomposition of indigo carmine and methylene blue dyes, as clarified in scheme 2. The holes interact with the negative hydroxide ions to form hydroxyl free radicals (OH.). Also, the electrons react with oxygen to form oxygen anion free radicals ($O_2.^-$). Besides, oxygen anion free radicals interact with hydrogen ions to form peroxide free radicals (HOO.), which turn into hydroxyl free radicals in the presence of ultraviolet light. Finally, the formed hydroxyl free radicals work to degrade the indigo carmine and methylene blue dyes and convert them into non-toxic gases such as carbon dioxide and water [25, 70–72]

To confirm the previous mechanism, ascorbic acid was used as a scavenger for electrons and oxygen anion free radicals. Also, ethylenediaminetetracetic acid disodium salt dihydrate and isopropyl alcohol were used as scavengers for holes and hydroxyl free radicals, respectively. Figure 8 A-B represents the relation between the decomposition percentage of indigo carmine and methylene blue dyes and scavengers, respectively. The photocatalytic decomposition percentage of methylene blue dye in the absence of scavengers is 93.03%. Besides, the photocatalytic decomposition percentage of methylene blue dye in the presence of ascorbic acid, ethylenediaminetetracetic acid disodium salt dihydrate, and isopropyl alcohol scavengers is 75.63, 48.44, and 26.90%, respectively. The photocatalytic decomposition percentage of indigo carmine dye in the absence of scavengers is 89.12%. Besides, the photocatalytic decomposition percentage of indigo carmine dye in the presence of ascorbic acid, ethylenediaminetetracetic acid disodium salt dihydrate, and isopropyl alcohol scavengers is 67.97, 39.45, and

Scheme 2 The mechanism of photocatalytic decomposition of methylene blue and indigo carmine dyes by the Li_3BO_3/CuO nanocomposite

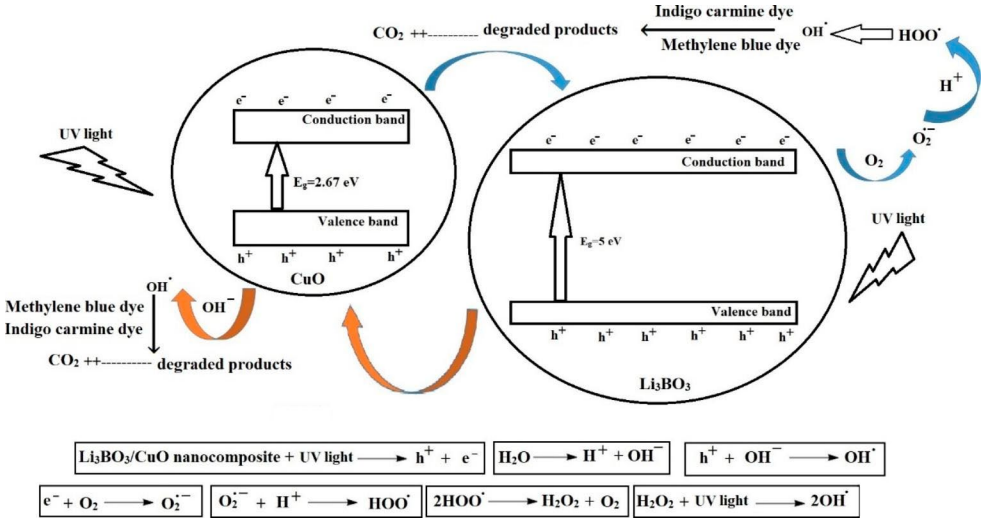

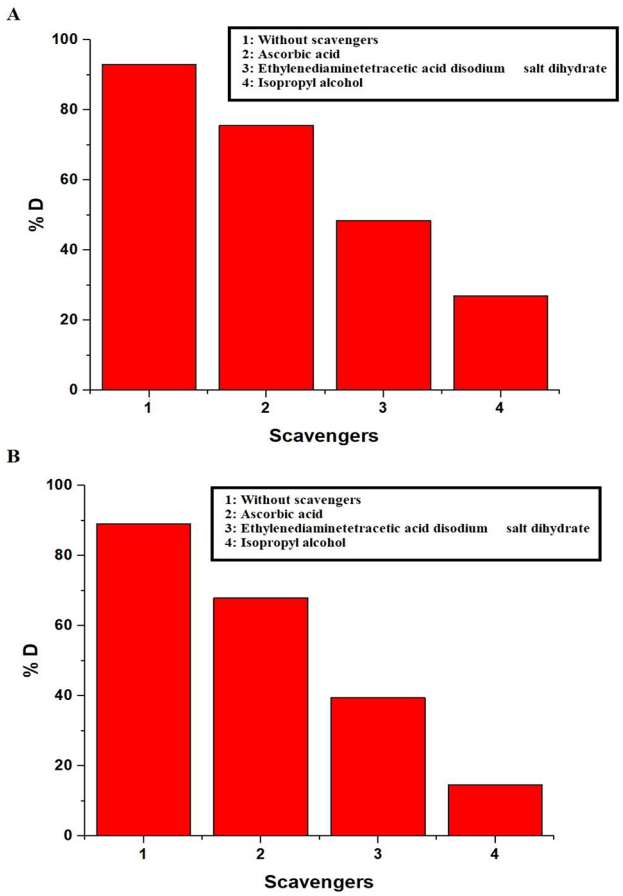

Fig. 8 The effect of scavengers on the decomposition percentage of 100 mL of 25 mg/L of methylene blue (**A**) and indigo carmine (**B**) dyes using 0.05 g of the synthesized nanocomposite

14.63%, respectively. Hence, the results proved that there was a decrease in the degradation percentage, which confirms the role of hydroxyl free radicals, oxygen anion free radicals, electrons, and holes in the decomposition of indigo carmine and methylene blue dyes, as shown in scheme 2 [70].

3.2.6 Comparison between the Photocatalytic Decomposition Percentage of Studied Dyes using the Li_3BO_3/CuO Nanocomposite and that of other Catalysts in the Literature

The decomposition percentage of methylene blue dye using the synthesized Li_3BO_3/CuO nanocomposite was compared with that of other catalysts in the literature such as, TiO_2/CeO_2 nanocomposite, CdS/TiO_2 nanocomposite, CeO_2/g-C_3N_4 composite, and Ca/ZnO composite, as shown in Table 1 [73–75]. In addition, the decomposition percentage of indigo carmine dye using the synthesized Li_3BO_3/CuO nanocomposite was compared with that of other catalysts in the literature such as, ZrO_2, ZrO_2/multiwalled carbon nanotube composite, ZnO, and $CoFe_2O_4/SnO_2$ composite, as shown in Table 2 [76–78]. As it is clear from the results, the synthesized nanocomposite has the highest efficiency.

4 Conclusions

Lithium borate/copper oxide nanocomposite was facilely synthesized using the pechini sol-gel chemical method for the efficient photocatalytic decomposition of indigo carmine and methylene blue dyes. The lithium borate/copper oxide nanocomposite was exposed to ultraviolet light, and hence electronic transitions occur from the valence band to the conduction band, which results in holes and electrons, which in turn produce free radicals that break down the indigo carmine and methylene blue dyes. The combination of lithium borate with copper oxide prevents fast recombination of holes/electrons and thus increases the efficiency of photocatalytic decomposition of indigo carmine and

Table 1 The decomposition percentage of methylene blue dye using the synthesized Li_3BO_3/CuO nanocomposite and other catalysts in the literature

Catalyst	Dose of catalyst (g)	Concentration of dye (mg/L)	Volume of dye (L)	% D	Time (min)	Ref
TiO_2/CeO_2 nanocomposite	0.15	10	100	47.52	120	[73]
CdS/TiO_2 nanocomposite	0.15	10	100	52.80	120	[73]
CeO_2/g-C_3N_4 composite	0.10	20	100	90.10	180	[74]
Ca/ZnO composite	0.25	10	100	40.00	140	[75]
Li_3BO_3/CuO nanocomposite	0.05	25	100	93.03	90	This work

Table 2 The decomposition percentage of indigo carmine dye using the synthesized Li_3BO_3/CuO nanocomposite and other catalysts in the literature

Catalyst	Dose of catalyst (g)	Concentration of dye (mg/L)	Volume of dye (L)	% D	Time (min)	Ref
ZrO_2	0.10	20	100	21.00	180	[76]
ZrO_2/multiwalled carbon nanotube composite	0.10	20	100	83.60	180	[76]
ZnO	0.10	20	100	17.70	210	[77]
$CoFe_2O_4$/SnO_2 composite	0.10	4.66	100	55	120	[78]
Li_3BO_3/CuO nanocomposite	0.05	25	100	89.13	90	This work

methylene blue dyes. The highest decomposition percentage of 100 mL of 25 mg/L of the methylene blue (at pH = 9) and indigo carmine (at pH = 3) dyes using 0.05 g of the synthesized nanocomposite are 93.03 and 89.13%, respectively.

Acknowledgements The authors are grateful to Princess Nourah bint Abdulrahman University, Riyadh, Saudi Arabia for funding this work through Researchers Supporting Project number (PNURSP2023R85).

Author Contributions N.S.A. (Experimental work- Research writing - Research review), F.A.S. (Preparing figures and tables), R.K.S. (Writing the introduction- Preparing figures and tables), G.S.E. (Experimental Work-Writing the Experimental), Z.A. (Response to the comments of reviewers-Revision of manuscript), E.A.A. (Idea, Experimental work, Research Writing). All authors reviewed and approved the final manuscript.

Funding The authors are grateful to Princess Nourah bint Abdulrahman University, Riyadh, Saudi Arabia for funding this work through Researchers Supporting Project number (PNURSP2023R85).

Declarations

Conflict of interest The authors confirm that there is no conflict of interest for this paper.

References

1. M. Ahmadian, M. Jaymand, Coord. Chem. Rev. **486**, 215152 (2023)
2. A. Kausar, S.T. Zohra, S. Ijaz, M. Iqbal, J. Iqbal, I. Bibi, S. Nouren, N. El, Messaoudi, A. Nazir, Int. J. Biol. Macromol. **224**, 1337 (2023)
3. M. Bilal, I. Ihsanullah, M.U. Hassan Shah, A.V. Bhaskar, Reddy, T.M. Aminabhavi, J. Environ. Manage. **321**, 115981 (2022)
4. S. Sankar Sana, R. Haldhar, J. Parameswaranpillai, M. Chavali, S.C. Kim, Clean. Mater. **6**, 100161 (2022)
5. T. He, Q. Li, T. Lin, J. Li, S. Bai, S. An, X. Kong, Y.F. Song, Chem. Eng. J. **462**, 142041 (2023)
6. G. Lin, B. Zeng, J. Li, Z. Wang, S. Wang, T. Hu, L. Zhang, Chem. Eng. J. 460, (2023)
7. N. Vasiraja, R. Saravana Sathiya, Prabhahar, A. Joshua, J. Clean. Prod. 397, (2023)
8. E.R. Kenawy, H. Tenhu, S.A. Khattab, A.A. Eldeeb, M.M. Azaam, Eur. Polym. J. **169**, 111138 (2022)
9. M. El-Kammah, E. Elkhatib, S. Gouveia, C. Cameselle, E. Aboukila, Sustain. Chem. Pharm. **29**, 100753 (2022)
10. M. Adel, M.A. Ahmed, A.A. Mohamed, Environ Nanatechnol. Monit Manag. **16**, 100550 (2021)
11. Y. Li, Y. An, R. Zhao, Y. Zhong, S. Long, J. Yang, J. Li, H. Zheng, Chemosphere. **296**, 134033 (2022)
12. M. Liu, W. Yin, T.L. Zhao, Q.Z. Yao, S.Q. Fu, G.T. Zhou, Sep. Purif. Technol. **272**, 118901 (2021)
13. S.K. Nataraj, K.M. Hosamani, T.M. Aminabhavi, Desalination. **249**, 12 (2009)
14. S. Ihaddaden, D. Aberkane, A. Boukerroui, D. Robert, J. Water Process. Eng. **49**, 102952 (2022)
15. E.A. Abdelrahman, R.M. Hegazey, S.H. Ismail, H.H. El-Feky, A.M. Khedr, M. Khairy, A.M. Ammar, Arab. J. Chem. **15**, 104372 (2022)
16. R.M. Hegazey, E.A. Abdelrahman, Y.H. Kotp, A.M. Hameed, A. Subaihi, J. Mater. Res. Technol. **9**, 1652 (2020)
17. E.A. Abdelrahman, R.M. Hegazey, Y.H. Kotp, A. Alharbi, Spectrochim. Acta - Part A Mol. Biomol. Spectrosc. **222**, 117195 (2019)

18. E.A. Abdelrahman, R.M. Hegazey, R.E. El-Azabawy, J. Mater. Res. Technol. **8**, 5301 (2019)
19. E.A. Abdelrahman, J. Mol. Liq. **253**, 72 (2018)
20. H. Gao, H. Yang, S. Wang, Optik (Stuttg). **175**, 237 (2018)
21. A.M. Alansi, M. Al-Qunaibit, I.O. Alade, T.F. Qahtan, T.A. Saleh, J. Mol. Liq. **253**, 297 (2018)
22. K. Sahu, S. kuriakose, J. Singh, B. Satpati, S. Mohapatra, J. Phys. Chem. Solids. **121**, 186 (2018)
23. A.S. Al-Wasidi, A.A. Almehizia, A.M. Naglah, H.M. Alkahtani, F.K. Algethami, E.S. Al-Farraj, M.T. Basha, E.A. Abdelrahman, Int. J. Environ. Anal. Chem. **00**, 1 (2022)
24. A.A. Almehizia, M.A. Al-Omar, A.M. Naglah, R.M. Hegazey, A.S. Al-Wasidi, H.A. Katouah, M.T. Basha, R.M. Alghanmi, A.M. Khedr, F.K. Algethami, E.A. Abdelrahman, Int. J. Environ. Anal. Chem. **00**, 1 (2022)
25. E.A. Abdelrahman, E.S. Al-Farraj, Nanomaterials. **12**, 3992 (2022)
26. P. Eskandari, E. Amarloo, H. Zangeneh, M. Rezakazemi, M.R. Zamani, T.M. Aminabhavi, J. Environ. Manage. **326**, 116691 (2023)
27. H. Niknam, A. Sadeghzadeh-Attar, Mater. Chem. Phys. **299**, 127489 (2023)
28. S. Kappadan, T.W. Gebreab, S. Thomas, N. Kalarikkal, Mater. Sci. Semicond. Process. **51**, 42 (2016)
29. A.S. Ganie, N. Bashar, S. Bano, S. Hijazi, S. Sultana, S. Sabir, M.Z. Khan, Surf. Interfaces. **38**, 102774 (2023)
30. S. Asadzadeh-Khaneghah, A. Habibi-Yangjeh, J. Clean. Prod. **276**, 124319 (2020)
31. H. Xiao, S. Liu, Mater. Des. **155**, 19 (2018)
32. G. Wang, Y. Jing, J. Ju, D. Yang, J. Yang, W. Gao, R. Cong, T. Yang, Inorg. Chem. **54**, 2945 (2015)
33. T. Harada, T.A. Hatton, J. Mater. Chem. A **5**, 22224 (2017)
34. N. Khalilzadeh, E. Bin Saion, H. Mirabolghasemi, K.A. Crouse, A.H. Bin, Shaari, and M. Bin Hashim, Results Phys. 5, 324 (2015)
35. X. Cui, F. Tang, C. Li, Y. Zhang, P. Wang, H. Feng, J. Zhao, F. Li, S. Li, Electrochim. Acta. **253**, 291 (2017)
36. A.H. Reshak, Phys. Chem. Chem. Phys. **19**, 30703 (2017)
37. A. Elaziouti, N. Laouedj, A. Bekka, R.N. Vannier, J. King Saud Univ. - Sci. **27**, 120 (2015)
38. V. Scuderi, G. Amiard, S. Boninelli, S. Scalese, M. Miritello, P.M. Sberna, G. Impellizzeri, V. Privitera, Mater. Sci. Semicond. Process. **42**, 89 (2016)
39. H. Li, Z. Su, S. Hu, Y. Yan, Appl. Catal. B Environ. **207**, 134 (2017)
40. Z. He, Y. Xia, B. Tang, X. Jiang, J. Su, Mater. Lett. **184**, 148 (2016)
41. C. Yerlikaya, N. Ullah, A.R. Kamali, R. Vasant Kumar, J. Therm. Anal. Calorim. **125**, 17 (2016)
42. B. Shojaei, R. Miri, A. Bazyari, L.T. Thompson, Fuel. **321**, 124136 (2022)
43. A. Alhaji, R.S. Razavi, A. Ghasemi, M.R. Loghman-Estarki, Ceram. Int. **43**, 2541 (2017)
44. A.S. Al, W. Faisal, K.A. Fawaz, A.S. Ehab, J. Inorg. Organomet. Polym. Mater. (2023)
45. A.S. Al-Wasidi, F.A. Saad, A.M. Munshi, E.A. Abdelrahman, RSC Adv. **13**, 5656 (2023)
46. A. Karami, R. Monsef, M.R. Shihan, L.Y. Qassem, M.W. Falah, M. Salavati-Niasari, Environ. Technol. Innov. **28**, 102947 (2022)
47. R. Monsef, M. Ghiyasiyan-Arani, M. Salavati-Niasari, ACS Appl. Energy Mater. **4**, 680 (2021)
48. M.A. Mahdi, S.R. Yousefi, L.S. Jasim, M. Salavati-Niasari, Int. J. Hydrogen Energy. **47**, 14319 (2022)
49. S.R. Yousefi, M. Ghanbari, O. Amiri, Z. Marzhoseyni, P. Mehdizadeh, M. Hajizadeh-Oghaz, M. Salavati-Niasari, J. Am. Ceram. Soc. **104**, 2952 (2021)
50. S.R. Yousefi, H.A. Alshamsi, O. Amiri, M. Salavati-Niasari, J. Mol. Liq. **337**, 116405 (2021)
51. S.R. Yousefi, A. Sobhani, H.A. Alshamsi, M. Salavati-Niasari, RSC Adv. **11**, 11500 (2021)
52. S.R. Yousefi, D. Ghanbari, M. Salavati-Niasari, M. Hassanpour, J. Mater. Sci. Mater. Electron. **27**, 1244 (2016)
53. P. Mehdizadeh, M. Jamdar, M.A. Mahdi, W.K. Abdulsahib, L.S. Jasim, S. Raheleh, Yousefi, M. Salavati-Niasari, Arab. J. Chem. **16**, 104579 (2023)
54. C. Villa-Pérez, P. Arneodo Larochette, D.B. Soria, F.C. Gennari, Chem. Eng. J. 450, (2022)
55. G.G. Welegergs, H.G. Gebretinsae, M.G. Tsegay, A. Bhardwaj, S. Mathur, T.G. Kebede, Z.Y. Nuru, S. Dube, M. Maaza, Opt. Mater. (Amst). **135**, 113247 (2023)
56. F.K. Algethami, A.S. Al, W. Eida, S. Al Farraj, H.A. Katouah, E.A. Abdelrahman, Discov. Nano (2023)
57. A.S. Al-wasidi, H.A. Katouah, F.A. Saad, E.A. Abdelrahman, (2023)
58. N.S. Al, K. Fawaz, A.S. Reem, K.S. Eida, S. Al Farraj, G.S. El, E.A. Abdelrahman, J. Inorg. Organomet. Polym. Mater. (2023)
59. A.S. Al-wasidi, M.T. Basha, R.M. Alghanmi, E.S. Al-farraj, E.A. Abdelrahman, (2023)
60. D.D. Ramteke, H.C. Swart, R.S. Gedam, Phys. B Condens. Matter. **480**, 111 (2016)
61. X. Wang, L. Andrews, Mol. Phys. **107**, 739 (2009)
62. S.G.R. S, P. E, H.A. Alhadlaq, R. Mohan, A. G, and, M. Ahamed, J. King Saud Univ. - Sci. **34**, 102092 (2022)
63. A.S. Al-Wasidi, A.M. Naglah, F.A. Saad, E.A. Abdelrahman, Arab. J. Chem. **15**, 104178 (2022)
64. A.S. Al-Wasidi, H.S. AlSalem, A.F. Alshalawi, A.M. Naglah, A. Al-Anwar, E.A. Abdelrahman, Arab. J. Chem. **15**, 104113 (2022)
65. A.S. Al-Wasidi, A.M. Naglah, F.A. Saad, E.A. Abdelrahman, Arab. J. Chem. **15**, 104010 (2022)
66. E.A. Abdelrahman, Y.G. Abou El-Reash, H.M. Youssef, Y.H. Kotp, R.M. Hegazey, J. Hazard. Mater. **401**, 123813 (2021)
67. E.A. Abdelrahman, R.M. Hegazey, Compos. Part. B Eng. **166**, 382 (2019)
68. E.A. Abdelrahman, R.M. Hegazey, Microchem J. **145**, 18 (2019)
69. M.A. Abdelwahab, S.M. El Rayes, M.M. Kamel, E.A. Abdelrahman, Int. J. Environ. Anal. Chem. **00**, 1 (2022)
70. A. Alharbi, R.K. Shah, A. Sayqal, A. Subaihi, A.A. Alluhaybi, F.K. Algethami, A.M. Naglah, A.A. Almehizia, H.A. Katouah, H.M. Youssef, Alexandria Eng. J. **60**, 2167 (2021)
71. O.P. Kumar, M. Ahmad, M.A. Nazir, A. Anum, M. Jamshaid, S.S.A. Shah, A. Rehman, Environ. Sci. Pollut Res. **29**, 35300 (2022)
72. O. Parkash Kumar, K. Shahzad, M. Ahmad, Shoaib Ahmad Shah, and A. ur Rehman. Inorg. Chem. Commun. **146**, 110002 (2022)
73. M. Mahamud, A.M. Taddesse, Y. Bogale, Z. Bezu, Mater. Res. Bull. **161**, 112176 (2023)
74. G. Song, Z. Chu, W. Jin, H. Sun, Chin. J Chem Eng. **23**, 1326 (2015)
75. K.S. Mamatha, M. Shashank, G. Nagaraju, H.M.S. Kumar, J. Indian Chem. Soc. **99**, 100744 (2022)
76. W.W. Anku, S.O.B. Oppong, S.K. Shukla, E.S. Agorku, P.P. Govender, Prog Nat. Sci. Mater. Int. **26**, 354 (2016)
77. E.S. Agorku, M.A. Mamo, B.B. Mamba, A.C. Pandey, A.K. Mishra, Mater. Sci. Semicond. Process. **33**, 119 (2015)
78. N. AbouSeada, M.A. Ahmed, M.G. Elmahgary, Mater. Sci. Energy Technol. **5**, 116 (2022)